Anisotropic magnetoresistance in the itinerant antiferromagnetic EuTiO_{3}

Kaveh Ahadi, Xuezeng Lu, Salva Salmani-Rezaie, Patrick B. Marshall, James M. Rondinelli, and Susanne Stemmer

Phys. Rev. B **99**, 041106 — Published 7 January 2019

DOI: 10.1103/PhysRevB.99.041106

Anisotropic Magnetoresistance in Itinerant, Antiferromagnetic $EuTiO_3$

Kaveh Ahadi[1)] [†], Xuezeng Lu[2)], Salva Salmani-Rezaie[1)], Patrick B. Marshall[1)], James M. Rondinelli[2)], and Susanne Stemmer[1)]

[1)] Materials Department, University of California, Santa Barbara, California 93106-5050, USA.

[2)] Department of Materials Science and Engineering, Northwestern University, Evanston, IL 60208-3108, USA.

[†] Corresponding author. Email: kahadi@mrl.ucsb.edu

Abstract

We report on measurements of the anisotropic magnetoresistance (AMR) of doped $EuTiO_3$. It is shown that the primary contribution to the AMR is the crystalline component, which depends on the relative orientation between the magnetic moments and the crystal axes. With increasing magnetic field, a four-fold crystalline AMR undergoes a change in its alignment with respect to the crystal axes. The results are discussed in the context the coupling between spin canting, electronic structure, and transport. We discuss the potential role of Weyl points in the band structure. At high fields, the AMR transitions to uniaxial symmetry, which is lower than that of the lattice, along with a cross-over from positive to negative magnetoresistance.

Spin-orbit coupling plays a central role in the anisotropic magnetoresistance (AMR) and anomalous Hall effect (AHE) [1] of itinerant ferromagnets and in materials with topologically non-trivial electronic states. While an elegant theoretical framework exists for the intrinsic AHE and its connection to the Berry curvature of the electronic bands [2-7], AMR remains comparatively less well understood. Recently, both AMR and AHE have also attracted significant attention in *anti*ferromagnetic metals and semiconductors [8, 9]. For example, significant AHEs in non-collinear antiferromagnets have been discovered [10-12]. Another phenomenon of recent interest is the potential coupling between the orientation of the Néel vector and the topology of the electronic states in antiferromagnets with symmetry-protected Dirac and/or Weyl points in their band structure [13, 14]. Both AHE and AMR can serve as signatures of such interactions [13-15].

Degenerately doped, antiferromagnetic $EuTiO_3$ is an interesting testbed for these ideas for several reasons. Despite a small net magnetization, it exhibits an intrinsic AHE that changes sign as a function of the carrier density [16-18]. This is indicative of the Fermi level being located near a Weyl point or an avoided crossing, which are sources of Berry curvature [5, 7]. Recent density functional calculations (DFT) show the presence of Weyl points, which are near the Fermi level for the doping concentration where the sign changes in the AHE are observed, in case of *ferro*magnetic order [17]. At zero applied fields, the Eu moments order antiferromagnetically (*G*-type) [19, 20] with a Néel temperature of ~6 K that is relatively insensitive to the amount of doping [17]. A collinear spin arrangement cannot give rise to Weyl points, because time reversal and inversion symmetry are both present. This can also be seen in DFT calculations (see Supplementary Information [21]). Under applied magnetic fields, however, the spins cant and produce a small net magnetization [17]. The Eu spin orientation can then couple to the moments of carriers in the Ti 3*d* bands. DFT shows Weyl points in the electronic structure for various canted spin configurations (see Supplementary Information [21]). These Weyl points move as a function of spin canting angle [21]. Additionally, the Zeeman splitting of the bands can be large in $EuTiO_3$. While not captured in zero-field DFT calculations shown in the Supplementary Information, Zeeman fields have been suggested as a mechanism to move existing Weyl points in the Brillouin zone [18] or even generate new ones [30]. While this may be reflected in the AHE [17, 18], studies of the AMR effect can provide more direct information about the Fermi surface symmetry [13] and changes under magnetic fields. In this Letter, we report AMR measurements of doped $EuTiO_3$, which have not yet been investigated previously. We show that the AMR is highly unusual as it shows multiple transitions with increasing magnetic field strength.

A 100-nm-thick $EuTiO_3$ film was grown by molecular beam epitaxy (MBE) on (001) $(La_{0.3}Sr_{0.7})(Al_{0.65}Ta_{0.35})O_3$ (LSAT) single crystals and doped with Sm, which introduces carriers into the Ti 3*d* bands. Details of the growth have been reported elsewhere [17, 31]. X-ray diffraction reciprocal space maps confirmed that the $EuTiO_3$ film was coherently strained to the LSAT substrate [21]. $EuTiO_3$ is tetragonal (space group *I*4*/mcm*) at low temperatures. The compressive in-plane strain imposed by the LSAT substrate promotes a single-domain film with the tetragonal *c*-axis oriented along the film normal. The mismatch strain on LSAT is too small to break spatial inversion symmetry [32]. Neutron diffraction showed antiferromagnetic ordering with a Néel temperature of 6.27±0.08 K [17]. At the Néel temperature, a resistance anomaly can be observed, indicating coupling between the magnetic order and the transport properties [17, 21]. The Néel temperature and the resistance anomaly are both suppressed by the application of magnetic fields of a few T [21, 31, 33, 34]. Measurements of the spontaneous

Hall effects as a function of carrier density were reported elsewhere [17, 31, 35]. Here, a Hall bar structure was fabricated using standard contact lithography techniques. The Hall carrier density and mobility at 2 K were 2.2×10^{20} cm^{-3} and 211 cm^{2}V^{-1}s^{-1}, respectively, and the film showed metallic behavior [21]. For the AMR characterization, the longitudinal resistance (R_{xx}) was measured at 2 K, while the applied magnetic field (B) was rotated in the plane of the film, unless stated otherwise. The Hall bar and current (I) were oriented along either along the $[100]_c$ or $[110]_c$ in-plane directions, respectively (see Fig. 1). Here, the subscript refers to the fact that we use the cubic, high-temperature unit cell for the indices. The tetragonal unit cell is rotated by 45° relative to the cubic cell [36]. All magnetotransport measurements were carried out using a Quantum Design Physical Property Measurement System (PPMS).

Figure 2 shows the normalized longitudinal resistance, $R_{xx}(B)/R_{xx}(0)$, measured along $[100]_c$, as a function of B, as B is rotated from out-of-plane (90°) to the in-plane (0°, $B \parallel I$). An abrupt transition from positive to negative differential magnetoresistance is observed at a critical field, B_c. As B is rotated towards the in-plane configuration, B_c decreases from 2.6 T (90°) to 1.2 T (0°, $B \parallel I$). Both forward and backward sweeps are shown and no hysteresis is observed. As noted previously, this transition is absent at higher doping densities [17]. Films with carrier densities $> 4\times10^{20}$ cm^{-3} only show negative magnetoresistance and the sign of the spontaneous Hall effects is reversed [17].

Figure 3 shows the AMR for B in-plane and $I \parallel [100]_c$. Here, θ is the angle between B and I (see Fig. 1). Figures 3(a-b) show R_{xx} for different values of B (0.25 T - 2 T) as a function of θ, which was varied between 0° and 180°. Figure 4 shows the data for selected values of B in polar graphs and in terms of the relative AMR, $\mathrm{AMR}(\%) = \frac{R_{xx}-R_{min}}{R_{min}} \times 100$, and for a full rotation ($\theta =$ 0° - 360°), to better show the AMR symmetry. At low fields ($B < 0.3$ T) R_{xx} is almost independent of θ [Fig. 3(a)]. At intermediate fields ($0.4\ \mathrm{T} < B < 0.75\ \mathrm{T}$) the magnetoresistance has approximately four-fold symmetry [Fig. 4(a)] and we denote it AMR(I). For AMR(I), the maxima of R_{xx} occur for B oriented along the magnetic easy axes, $<100>_C$ (or <110> in the notation of the tetragonal unit cell) [36]. Near $B = 0.8$ T, R_{xx} again becomes independent of θ [see Fig. 3(a)]. Another four-fold symmetric AMR [AMR(II)] appears at slightly higher fields ($B = 0.9$ T – 1 T) [see Figs. 3(a) and 4(b)]. The maxima of R_{xx} are narrower and occur for $B \parallel <110>_C$, i.e., AMR(II) is rotated by 45° relative to AMR(I). Both AMR(I) and AMR(II) are high for an antiferromagnet at such low fields [37]. For example, AMR(I) reaches ~1.25% at 0.5 T. Figure 3(b) and Figs. 4 (c,d) show the AMR at high fields (1 T – 2 T). R_{xx} smoothly develops from having maxima for $B \parallel <110>_C$ at $B = 1$ T to a two-fold symmetric AMR [AMR(III)] with R_{xx} maxima for $B \parallel [010]_C$ and $B \parallel [0\bar{1}0]_C$ as B is increased. At 2 T, the two-fold AMR(III) is fully established. The appearance of AMR(III) coincides with the sign change of the differential magnetoresistance at $B > B_c$ (see Fig. 2).

Figure 5 shows the AMR for B in-plane and $I \| [110]_c$, with θ again indicating the angle between B and I. Shown are polar graphs for a full rotation of θ for $B = 0.5$ T, 1 T, 1.3 T and 2 T. The AMR symmetries and sequences are similar to those for $I \| [100]_c$, except that the data in Fig. 5 are all rotated by 45° relative to those in Fig. 4.

We next discuss the results. AMR effects can contain both non-crystalline and crystalline contributions [38]. The non-crystalline component has two-fold symmetry (AMR $\propto \cos 2\theta_M$) and depends only on the angle between the magnetization and the current (θ_M), i.e., it is independent of the angle between the current and the crystal axes [38]. In contrast, the crystalline component depends on the angle between the Néel vector and a specific crystallographic direction. Here, the AMR is clearly dominated by the crystalline AMR. This can be seen from the polar graphs: changing the direction of the current by 45° (from $[100]_c$ to $[110]_c$) produces a corresponding rotation in the polar AMR plot (Figs. 4 and 5). This shows that R_{xx} is determined by the angle between the crystal axes and the Néel vector, i.e., it is not the conventional, scattering-related AMR of an antiferromagnet (see, e.g., ref. [37]). For $EuTiO_3$, a four-fold symmetric crystalline AMR is expected based on the in-plane symmetry of the tetragonal, c-axis oriented film, constrained to a cubic substrate, explaining the four-fold AMR(I). The fact that AMR(I) appears around 0.3 T indicates that this field is sufficient to re-orient the Néel vector. The low B value is consistent with the spin flop field reported for $EuTiO_3$ single crystals [34, 39]. We note that AMR(I) is not perfectly four-fold, since the relative AMR is slightly larger for $B \parallel I$. This may indicate the presence of an additional two-fold component. Like AMR(I), the four-fold AMR(II) and the two-fold (uniaxial) AMR(III) are crystalline AMRs. A remarkable observation here is the uniaxial AMR(III), because it is lower in symmetry than the tetragonal, *c*-axis oriented film, with in-plane lattice parameters that are constrained to the cubic substrate.

Magnetic field-induced changes in the AMR symmetry are unusual. They have been reported for Sr_2IrO_4 [40, 41], where magnetoelastic effects have been suggested as the origin [40]. Here, the strain state of the film is dominated by in-plane compressive strain from the substrate, which can determine magnetic anisotropies [42], but is not expected to change as a function of the magnetic field. Magnetic field induced changes in the AMR have also been observed in Dirac semimetals, such as $ZrTe_5$, and attributed topological phase transitions caused by Weyl points that move under the magnetic field [43]. Weyl points also appear in the band structure of $EuTiO_3$ [21]. Specifically, as discussed above, the applied magnetic field controls both the spin canting as well as Zeeman splitting, and thus the presence and location of the Weyl points. Furthermore, the transition from AMR(I) to AMR(II) appears in conjunction with the unusual (non-monotonic) behavior of the spontaneous Hall effects reported in prior studies [17, 31]. It is therefore possible that changes in the electronic structure explain the observed transition from AMR(I) to AMR(II).

The transition to AMR(III) is even more remarkable and unexpected. This two-fold "crystalline" AMR likely cannot be explained with the effects of spin canting on the electronic structure, which should retain the four-fold symmetry. The lower AMR symmetry indicates a new phase that is induced as the antiferromagnetic order breaks down. The uniaxial AMR symmetry is lower than the symmetry of the lattice and reminiscent of magnetic-field induced nematicity found in other systems [44]. It is correlated with an abrupt transition of the differential magnetoresistance from positive to negative, which is indicative of spin fluctuation scattering. The fact that this is only observed within a certain doping range again points to the importance of the underlying electronic structure [17]. We have previously noted that at the same field, indications of a quantum critical point exist [17]. Future studies of the magnetic structures of doped films as a function of magnetic field would be helpful in developing a quantitative picture of this phase and the transitions in the AMR observed here.

Acknowledgments

The authors gratefully acknowledge discussions with Leon Balents and Libor Šmejkal. The authors acknowledge support by the National Science Foundation (grant nos. 1729303 and 1729489) and by a MURI program of the Army Research Office (Grant No. W911NF-16-1-0361). The work made use of the MRL Shared Experimental Facilities, which are supported by the MRSEC Program of the U.S. National Science Foundation under Award No. DMR 1720256.

References

[1] R. Karplus, and J. M. Luttinger, Phys. Rev. **95**, 1154 (1954).

[2] M. Onoda, and N. Nagaosa, J. Phys. Soc. Jpn. **71**, 19 (2002).

[3] J. W. Ye, Y. B. Kim, A. J. Millis, B. I. Shraiman, P. Majumdar, and Z. Tesanovic, Phys. Rev. Lett. **83**, 3737 (1999).

[4] F. D. M. Haldane, Phys. Rev. Lett. **93**, 206602 (2004).

[5] Z. Fang, N. Nagaosa, K. S. Takahashi, A. Asamitsu, R. Mathieu, T. Ogasawara, H. Yamada, M. Kawasaki, Y. Tokura, and K. Terakura, Science **302**, 92 (2003).

[6] D. Xiao, M. C. Chang, and Q. Niu, Rev. Mod. Phys. **82**, 1959 (2010).

[7] X. J. Wang, J. R. Yates, I. Souza, and D. Vanderbilt, Phys. Rev. B **74**, 195118 (2006).

[8] L. S□mejkal, Y. Mokrousov, B. Yan, and A. H. MacDonald, Nat. Phys. **14**, 242 (2018).

[9] M. B. Jungfleisch, W. Zhang, and A. Hoffmann, Phys. Lett. A **382**, 865 (2018).

[10] H. Chen, Q. Niu, and A. H. MacDonald, Phys. Rev. Lett. **112**, 017205 (2014).

[11] J. Kubler, and C. Felser, Epl **108**, 67001 (2014).

[12] S. Nakatsuji, N. Kiyohara, and T. Higo, Nature **527**, 212 (2015).

[13] L. Smejkal, J. Zelezny, J. Sinova, and T. Jungwirth, Phys. Rev. Lett. **118**, 106402 (2017).

[14] J. P. Liu, and L. Balents, Phys. Rev. Lett. **119**, 087202 (2017).

[15] T. Suzuki, R. Chisnell, A. Devarakonda, Y. T. Liu, W. Feng, D. Xiao, J. W. Lynn, and J. G. Checkelsky, Nat. Phys. **12**, 1119 (2016).

[16] K. S. Takahashi, M. Onoda, M. Kawasaki, N. Nagaosa, and Y. Tokura, Phys. Rev. Lett. **103**, 057204 (2009).

[17] K. Ahadi, Z. G. Gui, Z. Porter, J. W. Lynn, Z. J. Xu, S. D. Wilson, A. Janotti, and S. Stemmer, APL Mater. **6**, 056105 (2018).

[18] K. S. Takahashi, H. Ishizuka, T. Murata, Q. Y. Wang, Y. Tokura, N. Nagaosa, and M. Kawasaki, Sci. Adv. **4**, eaar7880 (2018).

[19] C. L. Chien, S. Debenedetti, and F. D. S. Barros, Phys. Rev. B **10**, 3913 (1974).

[20] T. R. McGuire, M. W. Shafer, R. J. Joenk, H. A. Alperin, and S. J. Pickart, J. Appl. Phys. **37**, 981 (1966).

[21] See supplementary Information [link to be inserted by publisher], which also includes refs. [22-29] for density functional calculations of the d-bands for different spin alignments, a cross-section scanning transmission electron microscopy image, a reciprocal space map, and the transport proporties as a function of temperature.

[22] J. P. Perdew, A. Ruzsinszky, G. I. Csonka, O. A. Vydrov, G. E. Scuseria, L. A. Constantin, X. L. Zhou, and K. Burke, Phys. Rev. Lett. **100**, 136406 (2008).

[23] G. Kresse, and J. Furthmuller, Phys. Rev. B **54**, 11169 (1996).

[24] G. Kresse, and J. Furthmüller, Comp. Mater. Sci. **6**, 15 (1996).

[25] G. Kresse, and D. Joubert, Phys. Rev. B **59**, 1758 (1999).

[26] P. E. Blochl, Phys. Rev. B **50**, 17953 (1994).

[27] A. I. Liechtenstein, V. I. Anisimov, and J. Zaanen, Phys. Rev. B **52**, R5467(R) (1995).

[28] R. Ranjan, H. S. Nabi, and R. Pentcheva, J. Phys. Cond. Mat. **19**, 406217 (2007).

[29] P. J. Ryan, J.-W. Kim, T. Birol, P. Thompson, J.-H. Lee, X. Ke, P. S. Normile, E. Karapetrova, P. Schiffer, S. D. Brown, C. J. Fennie, and D. G. Schlom, Nat. Comm. **4**, 1334 (2013).

[30] D. Gresch, Q. Wu, G. W. Winkler, and A. A. Soluyanov, New J. Phys. **19**, 035001 (2017).

[31] K. Ahadi, L. Galletti, and S. Stemmer, Appl. Phys. Lett. **111**, 172403 (2017).

[32] J. H. Lee, L. Fang, E. Vlahos, X. L. Ke, Y. W. Jung, L. F. Kourkoutis, J. W. Kim, P. J. Ryan, T. Heeg, M. Roeckerath, V. Goian, M. Bernhagen, R. Uecker, P. C. Hammel, K. M. Rabe, S. Kamba, J. Schubert, J. W. Freeland, D. A. Muller, C. J. Fennie, P. Schiffer, V. Gopalan, E. Johnston-Halperin, and D. G. Schlom, Nature **466**, 954 (2010).

[33] T. Katsufuji, and Y. Tokura, Phys. Rev. B **60**, R15021 (1999).

[34] A. P. Petrovic, Y. Kato, S. S. Sunku, T. Ito, P. Sengupta, L. Spalek, M. Shimuta, T. Katsufuji, C. D. Batista, S. S. Saxena, and C. Panagopoulos, Phys. Rev. B **87**, 064103 (2013).

[35] K. Ahadi, H. Kim, and S. Stemmer, APL Mater. **6**, 056102 (2018).

[36] V. Scagnoli, M. Allieta, H. Walker, M. Scavini, T. Katsufuji, L. Sagarna, O. Zaharko, and C. Mazzoli, Phys. Rev. B **86**, 094432 (2012).

[37] X. Marti, I. Fina, C. Frontera, J. Liu, P. Wadley, Q. He, R. J. Paull, J. D. Clarkson, J. Kudrnovsky, I. Turek, J. Kunes, D. Yi, J. H. Chu, C. T. Nelson, L. You, E. Arenholz, S. Salahuddin, J. Fontcuberta, T. Jungwirth, and R. Ramesh, Nat. Mater. **13**, 367 (2014).

[38] D. Kriegner, K. Vyborny, K. Olejnik, H. Reichlova, V. Novak, X. Marti, J. Gazquez, V. Saidl, P. Nemec, V. V. Volobuev, G. Springholz, V. Holy, and T. Jungwirth, Nat. Commun. **7**, 11623 (2016).

[39] A. Midya, P. Mandal, K. Rubi, R. F. Chen, J. S. Wang, R. Mahendiran, G. Lorusso, and M. Evangelisti, Phys. Rev. B **93**, 094422 (2016).

[40] C. Wang, H. Seinige, G. Cao, J. S. Zhou, J. B. Goodenough, and M. Tsoi, Phys. Rev. X **4**, 041034 (2014).

[41] C. L. Lu, B. Gao, H. W. Wang, W. Wang, S. L. Yuan, S. Dong, and J. M. Liu, Adv. Funct. Mater. **28**, 1706589 (2018).

[42] X. Ke, T. Birol, R. Misra, J. H. Lee, B. J. Kirby, D. G. Schlom, C. J. Fennie, and J. W. Freeland, Phys. Rev. B **88**, 094434 (2013).

[43] G. Zheng, X. Zhu, Y. Liu, J. Lu, W. Ning, H. Zhang, W. Gao, Y. Han, J. Yang, H. Du, K. Yang, Y. Zhang, and M. Tian, Phys. Rev. B **96**, 121401(R) (2017).

[44] R. A. Borzi, S. A. Grigera, J. Farrell, R. S. Perry, S. J. S. Lister, S. L. Lee, D. A. Tennant, Y. Maeno, and A. P. Mackenzie, Science **315**, 214 (2007).

Figure Captions

Figure 1: Schematic showing the Hall bar structure used for the AMR measurements.

Figure 2: R_{xx}, normalized to the resistance at zero applied field (R_0), as a function of magnetic field B for $I \parallel [100]_C$, measured at 2 K. R_{xx} was symmetrized to eliminate the transverse resistance contribution. The labels indicate the out-of-plane angle between I and B.

Figure 3: AMR for for $I \parallel [100]_C$ measured at 2 K. Shown is R_{xx} for different in-plane applied magnetic fields (see labels). The in-plane angle θ (see Fig. 1) was varied between 0° and 180°.

Figure 4: AMR for for $I \parallel [100]_C$ measured at 2 K. Shown is the relative AMR given in % plotted using polar graphs under different applied fields (see labels). The in-plane angle θ is varied between 0° and 360°.

Figure 5: AMR for for $I \parallel [110]_C$ measured at 2 K. Shown is the relative AMR given in % plotted using polar graphs under different applied fields (see labels). The in-plane angle θ is varied between 0° and 360°.

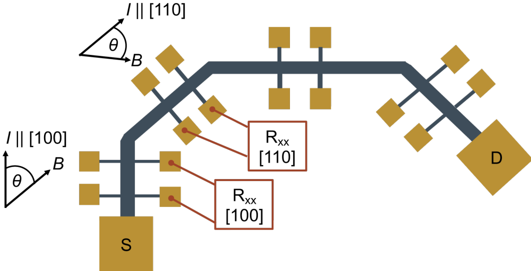

$I \parallel [110]$
θ
B
$I \parallel [100]$
B
θ
R_{xx} [110]
R_{xx} [100]
D
S

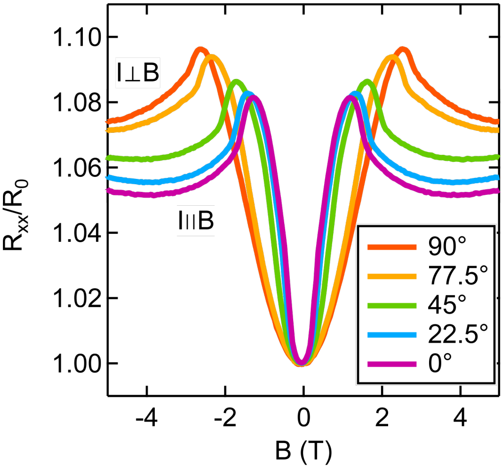

1.10
1.08
1.06
1.04
1.02
1.00
R_{xx}/R_0
I⊥B
I∥B
90°
77.5°
45°
22.5°
0°
-4
-2
0
2
4
B (T)

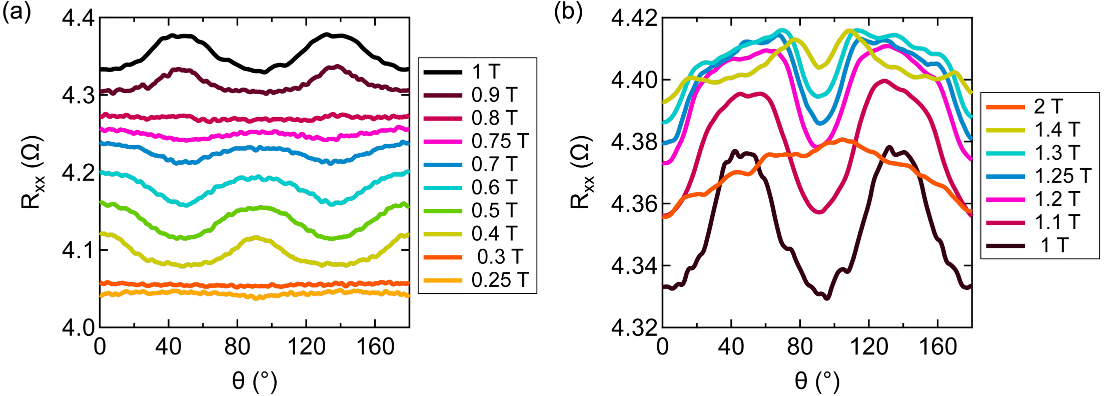
(a)
4.4
4.3
4.2
4.1
4.0
R_xx (Ω)
0
40
80
120
160
θ (°)
1 T
0.9 T
0.8 T
0.75 T
0.7 T
0.6 T
0.5 T
0.4 T
0.3 T
0.25 T
(b)
4.42
4.40
4.38
4.36
4.34
4.32
R_xx (Ω)
0
40
80
120
160
θ (°)
2 T
1.4 T
1.3 T
1.25 T
1.2 T
1.1 T
1 T

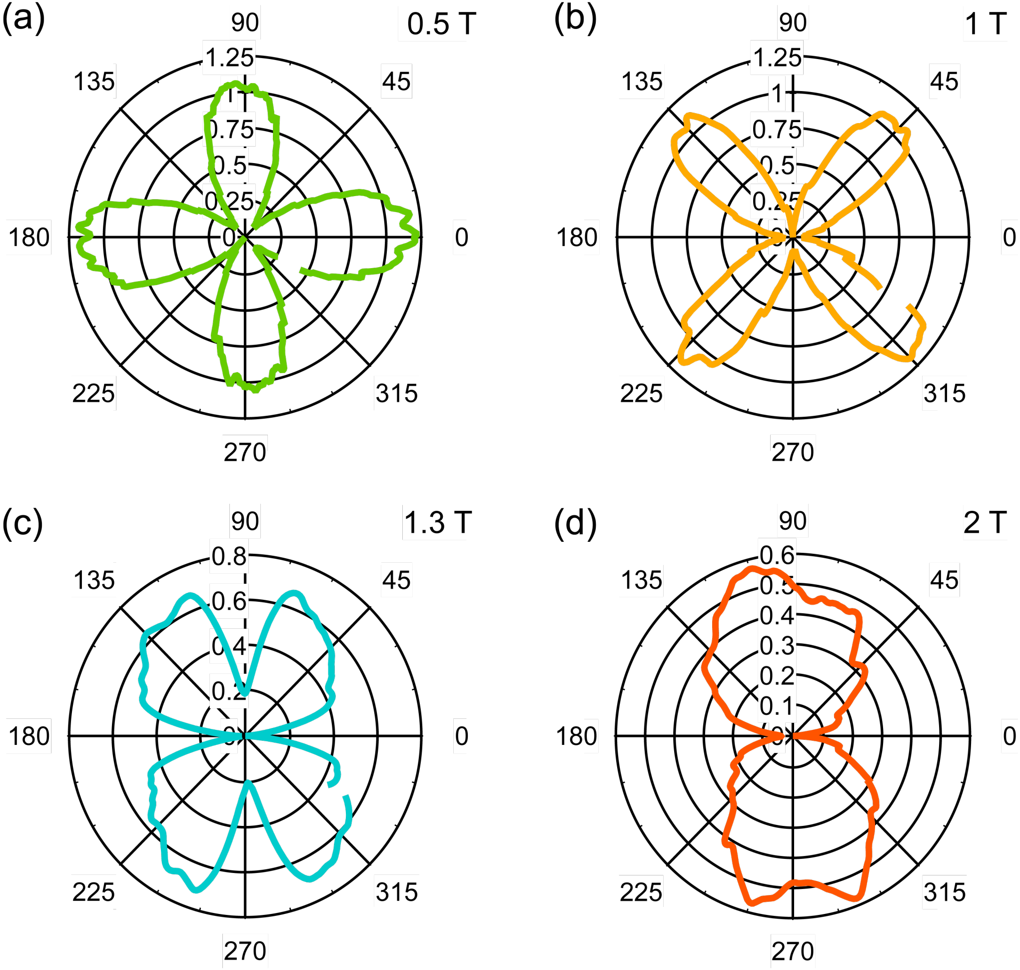
(a)
0.5 T
90
45
0
315
270
225
180
135
1.25
1
0.75
0.5
0.25
0
(b)
1 T
90
45
0
315
270
225
180
135
1.25
1
0.75
0.5
0.25
0
(c)
1.3 T
90
45
0
315
270
225
180
135
0.8
0.6
0.4
0.2
0
(d)
2 T
90
45
0
315
270
225
180
135
0.6
0.5
0.4
0.3
0.2
0.1
0

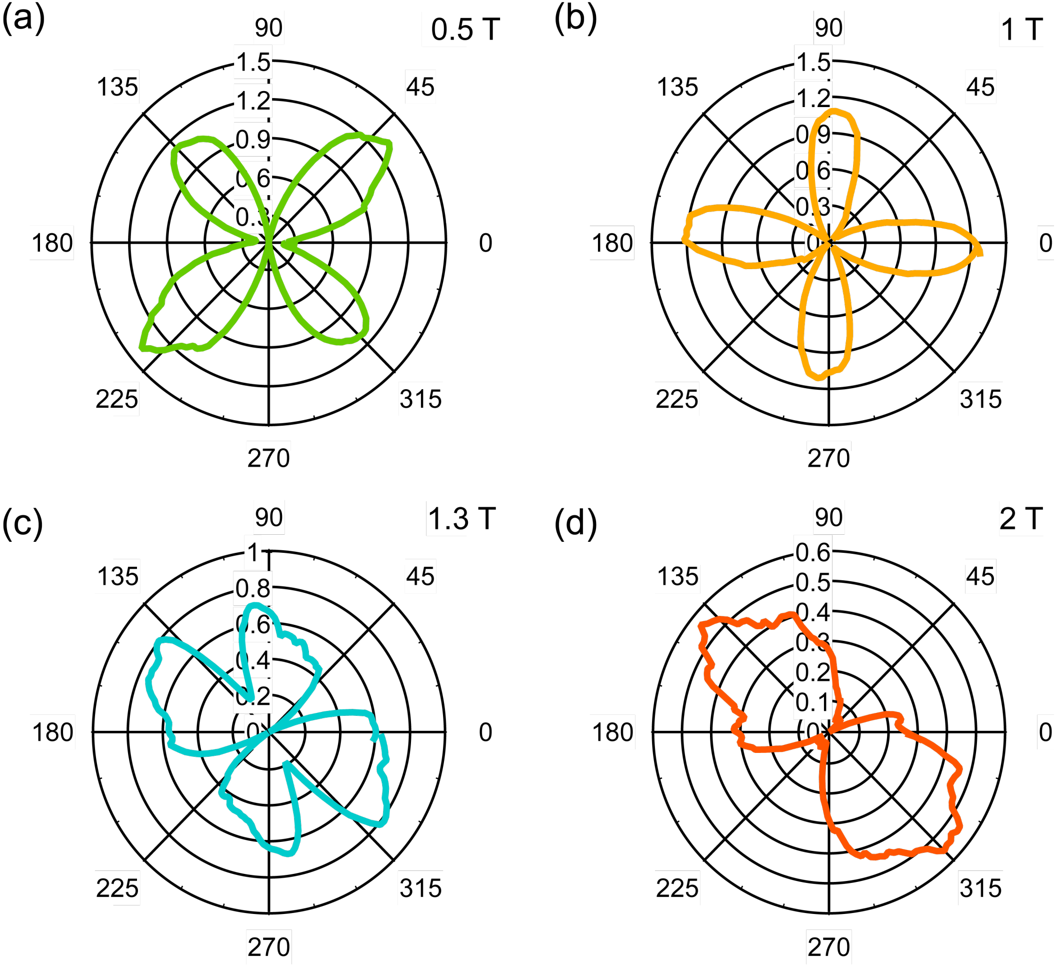
(a)
0.5 T
90
45
0
315
270
225
180
135
1.5
1.2
0.9
0.6
0.3
(b)
1 T
90
45
0
315
270
225
180
135
1.5
1.2
0.9
0.6
0.3
0
(c)
1.3 T
90
45
0
315
270
225
180
135
1
0.8
0.6
0.4
0.2
0
(d)
2 T
90
45
0
315
270
225
180
135
0.6
0.5
0.4
0.3
0.2
0.1
0